Application of the k-ε-v^2 model to multi-component airfoils

By G. Iaccarino[1] AND P. A. Durbin[2]

Flow computations around two-element and three-element configurations are presented and compared to detailed experimental measurements. The $k-\varepsilon-\overline{v^2}$ model has been applied and the ability of the model to capture streamline curvature effects, wake-boundary layer confluence, and laminar/turbulent transition is discussed. The numerical results are compared to experimental datasets that include mean quantities (velocity and pressure coefficient) and turbulent quantities (Reynolds normal and shear stresses).

1. Introduction

An accurate prediction of turbulent flow over a wing is still a challenging problem. Even a two-dimensional computation over a multi-element airfoil close to the maximum lift is an unsolved problem due to the complex geometry producing complicated viscous flow.

Within the aircraft industry the design of high-lift devices is an important topic which can have a major influence on the overall economy and safety of the aircraft. Therefore, development and improvements of numerical tools capable of handling separated viscous flows are of great interest. Computational methods for the design of high-lift systems are, traditionally, based on the viscous-inviscid interaction approach with integral methods for boundary layers and wakes.

Today, due to developments in computer technology and improvements in numerical algorithms, there is a renewed interest in the possibility of obtaining Reynolds averaged Navier-Stokes solutions for high-lift flows. The main open topics in this field of application are grid generation and turbulence modeling. The first one has been addressed and partially solved with the introduction of the *zonal* methods. By this way, the computational domain is divided into zones and the mesh and solutions are computed independently; the matching conditions between different regions provide boundary conditions for the zones. In particular, multiple-zones meshes can be either patched (pointwise continuous) or *chimera* (overlapping) grids. The use of unstructured grids is another interesting answer to this problem and is still under development for viscous applications.

1 CIRA, Centro Italiano Ricerche Aerospaziali, Italy
2 Stanford University

The other crucial point is the handling of the turbulence for such a complicated flow situation. There is no shortage of numerical methods to take into account turbulent fluctuations when solving Reynolds Averaged Navier-Stokes (RANS) equations based either on algebraic or differential equations. It is only the effectiveness of the models that is at issue.

2. Numerical model

2.1 RANS flow solver

The numerical method is based on an extended version of the incompressible Navier-Stokes two-dimensional (INS2D) code of Rogers and Kwak (Rogers, 1991). The incompressible, Reynolds Averaged Navier Stokes equations are solved by an artificial compressibility method. The basic technique is based on cell-vertex finite differences over structured meshes. The spatial discretization scheme is a third-order upwind biased for convective contributions and second-order centered for diffusive terms. The time integration is implicit and the equations are solved in a coupled way. The implicit matrices are inverted by ADI line relaxations.

2.2 Turbulence modeling

The turbulence model is based in part on the standard $k-\varepsilon$ equations:

$$\partial_t k + U\cdot\nabla k = P_k - \varepsilon + \nabla\cdot[(\nu + \frac{\nu_t}{\sigma_k})\nabla k], \tag{1}$$

$$\partial_t \varepsilon + U\cdot\nabla \varepsilon = \frac{C_{\epsilon 1}P_k - C_{\epsilon 2}\varepsilon}{T} + \nabla\cdot[(\nu + \frac{\nu_t}{\sigma_\epsilon})\nabla \varepsilon]. \tag{2}$$

Another transport equation is introduced to model near-wall effects and the anisotropy of the Reynolds stresses. This reads as

$$\partial_t \overline{v^2} + U\cdot\nabla \overline{v^2} = kf - \overline{v^2}\frac{\varepsilon}{k} + \nabla\cdot[(\nu+\nu_t)\nabla\overline{v^2}], \tag{3}$$

where $\overline{v^2}$ can be regarded as the turbulent intensity normal to streamlines and kf, the production of $\overline{v^2}$, accounts for the redistribution of turbulence intensity from the streamwise component. By using this equation 'wall-echo' effects are automatically taken into account. The production of $\overline{v^2}$ is modeled by means of an elliptic relaxation equation for f (Durbin, 1991)

$$L^2\nabla^2 f - f = \frac{1}{T}(C_1 - 1)\left[\frac{\overline{v^2}}{k} - \frac{2}{3}\right] - C_2\frac{P_k}{k}. \tag{4}$$

In the previous equations time and length scales are computed as

$$T = \max\left[\frac{k}{\varepsilon}, 6(\frac{\nu}{\varepsilon})^{1/2}\right],\ L = C_L\max\left[\frac{k^{3/2}}{\varepsilon}, C_\eta(\frac{\nu^3}{\varepsilon})^{1/4}\right]. \tag{5}$$

The treatment of the wall boundary conditions for the turbulent quantities is based on the asymptotic behavior of k and $\overline{v^2}$. As $y \to 0$

$$k = 0, \; k \to y^2 \frac{\epsilon}{2\nu}, \tag{6}$$

$$\overline{v^2} = 0, \; \overline{v^2} \to -y^4 \epsilon \frac{f}{20\nu^2}. \tag{7}$$

The eddy viscosity is given by

$$\nu_t = C_\mu \overline{v^2} T. \tag{8}$$

The constants of the model are:

$$C_\mu = 0.19, \; \sigma_k = 1, \; \sigma_\epsilon = 1.3,$$

$$C_{\epsilon 1} = 1.55, \; C_{\epsilon 2} = 1.9$$

$$C_1 = 1.4, \; C_2 = 0.3, \; C_L = 0.3, \; C_\eta = 70. \tag{9}$$

The space discretization of Eqs. (1) to (4) is the same used for the mean flow and the time integration is based on the same implicit procedure. The equations are solved as a coupled two-by-two block tridiagonal system (the mean flow is solved as a coupled three-by-three system).

3. Two-component configuration

3.1 Experimental test conditions

The experimental test was conducted in the $7x10$" wind tunnel at NASA Ames Research Center, Moffett Field, California (Adair, 1989). The airfoil/flap configuration includes a NACA 4412 main airfoil section equipped with a NACA 4415 flap airfoil section. The geometric location of the flap was specified by the flap gap (FG), the flap overlap (FO), and the flap deflection (δ_f). In this work, we are using $FG = 0.035c$, $FO = 0.028c$ and $\delta_f = 21.8^o$, where c is the chord length of the main airfoil. The angle of attack was set to $\alpha = 8.2^o$ and flow conditions were specified as Mach number $M = 0.09$ and Reynolds number $Re = 1.8 \times 10^6$. Two-dimensionality of the measurements was ensured by using fences, and the transition to turbulence was enforced by using trips at the main airfoil leading edge and at the suction side of the flap close to the flap pressure minimum.

3.2 Numerical test conditions

A two-dimensional model is used for the computations; it represents the midspan section of the experimental set-up. The airfoil configuration was characterized by the value of FG, FO, and δ_f indicated previously. The presence of the wind-tunnel walls was taken into account because of the large blocking effects, as was recommended by the experimental investigators (Adair, 1989); for simplicity, slip boundary conditions were imposed on the wind-tunnel walls. The inlet and outlet sections were set at 5 chords upwind and 15 chords downwind respectively to minimize their effects on the computed flow field. The angle of attack and the Reynolds

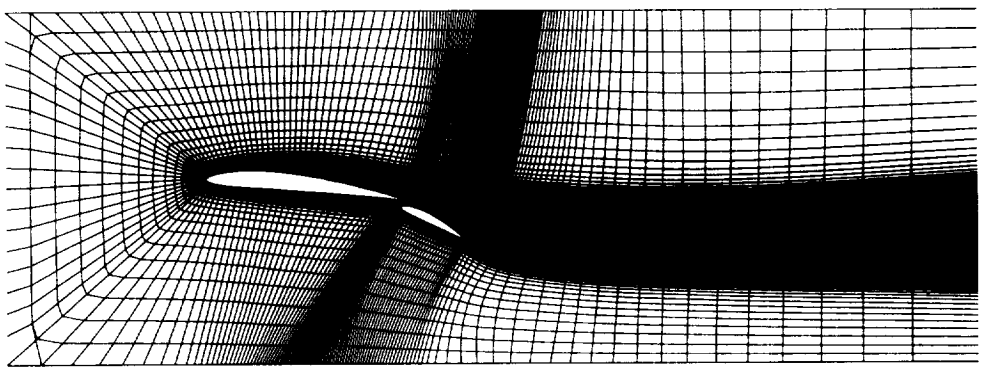

FIGURE 1. View of the computational grid.

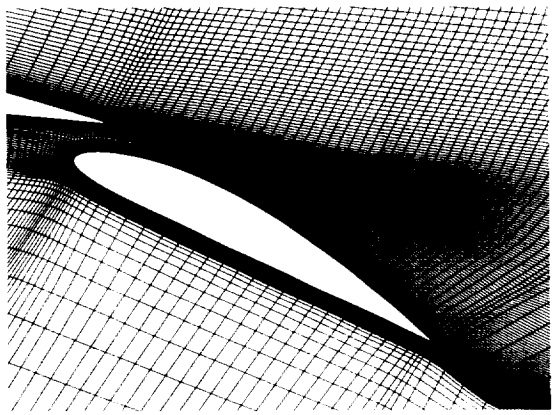

FIGURE 2. Close-up of the grid around the flap.

number were the same as the experiments, while the flow was assumed to be incompressible. Transition trips were not accounted for: the flow is considered to have a very low turbulence intensity at the wind tunnel inlet, and the model is allowed to undergo its natural, bypass transition.

The computational grid was generated by FFA (Sweden Research Center) under the auspices of the GARTEUR Action Group AG-25. A general view of mesh is reported in Fig. 1, while a close-up of the grid around the flap is given in Fig. 2. Due to the complexity of the geometry the computational grid was generated via a multiblock approach; seven zones were created allowing very good resolution of the mesh close to the airfoils (a C-type grid); about 100,000 total grid points were used. The square trailing edges of both airfoils were also retained (see Fig. 2) even though the resolution in the streamwise direction is quite limited.

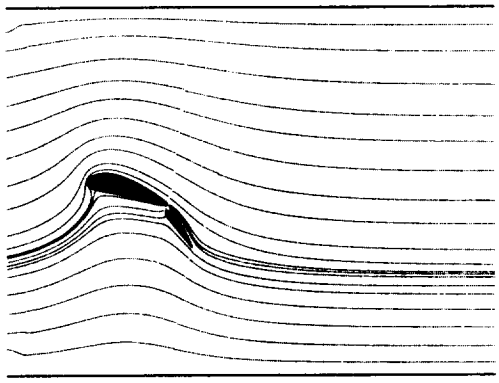

FIGURE 3. Computed streamlines.

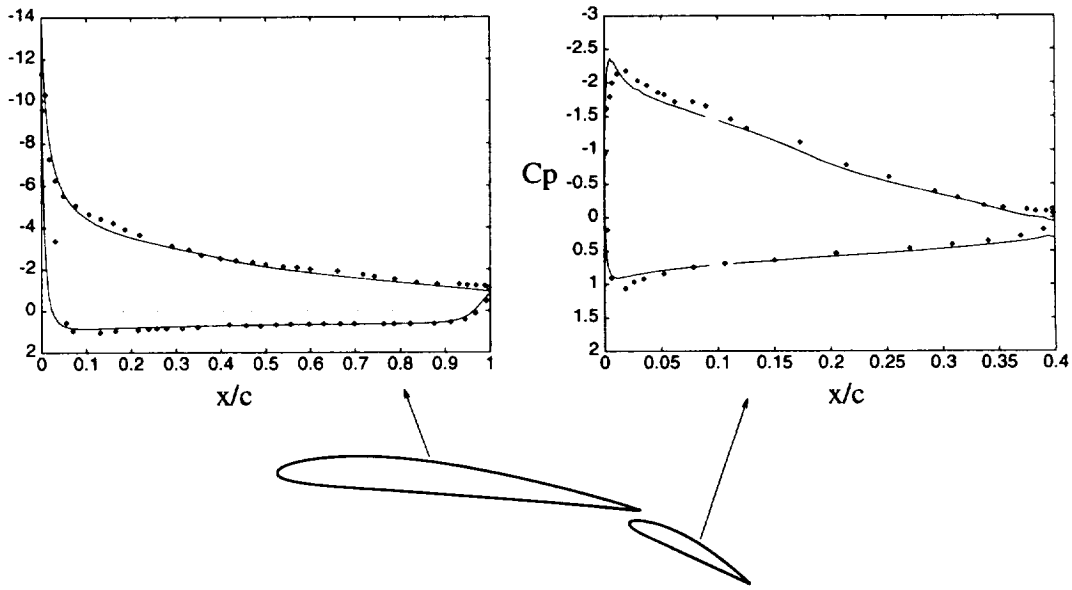

FIGURE 4. Pressure distributions on the airfoil surface. ——— : computed results; ◊: measured data.

3.3 Results

The characterization of the flow field is reported in Fig. 3 by means of the streamlines. Only a portion of the flow domain is shown. The blocking effect of the wind tunnel walls and the large curvature of the wake downstream of the flap are evident. A little separation bubble is also present at the flap trailing edge, in accord with the experimental findings.

3.3.1 Mean flow: pressure

The comparison between computed and measured pressure coefficient is reported

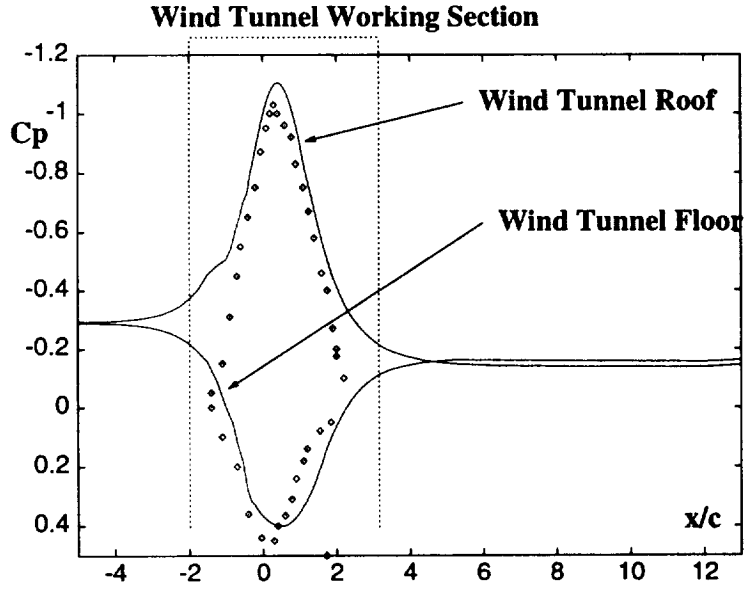

FIGURE 5. Pressure distributions on the wind tunnel walls. ——— : computed results; ◊: measured data.

in Fig. 4. These results can be compared to those published by Rogers *et al.* (1993).

The agreement is quite satisfactory for both the main airfoil and the flap. The suction peak is very well captured on the main airfoil although the stagnation point is completely misplaced. This is probably due to three-dimensional effects in the experimental test as can be seen from Fig. 3 of (Adair, 1987). Another reasonable explanation for this discrepancy is a difference between the geometric location of the airfoil/flap configuration in the experimental and numerical models. It is worth noting that the numerical results of Rogers (1993) show this same discrepancy in the location of the stagnation point. We point out that the geometry definition of the airfoil/flap configuration (in terms of FG, FO, and δ_f) is somewhat confusing and this could have led to a different shape of the slot in the numerical and experimental models.

The pressure peak over the flap is overpredicted and, in particular, located upstream with respect to the experimental one. The numerical model fails to capture the correct pressure plateau at the trailing edge of the flap and, therefore, the separation region. In particular, the separation point is well captured (it is located at 7% upstream of the trailing edge) as is shown in Fig. 4, but the maximum height of the recirculation bubble is underpredicted.

In Fig. 5, the pressure distribution over the wind tunnel walls is reported and compared to the experimental findings. On the working section roof, the agreement is satisfactory even though an overprediction of the pressure level is present. On the other hand, at the floor, a shift in the pressure distribution is observed. However, the grid resolution in the region is quite coarse. Note that as the inlet and the

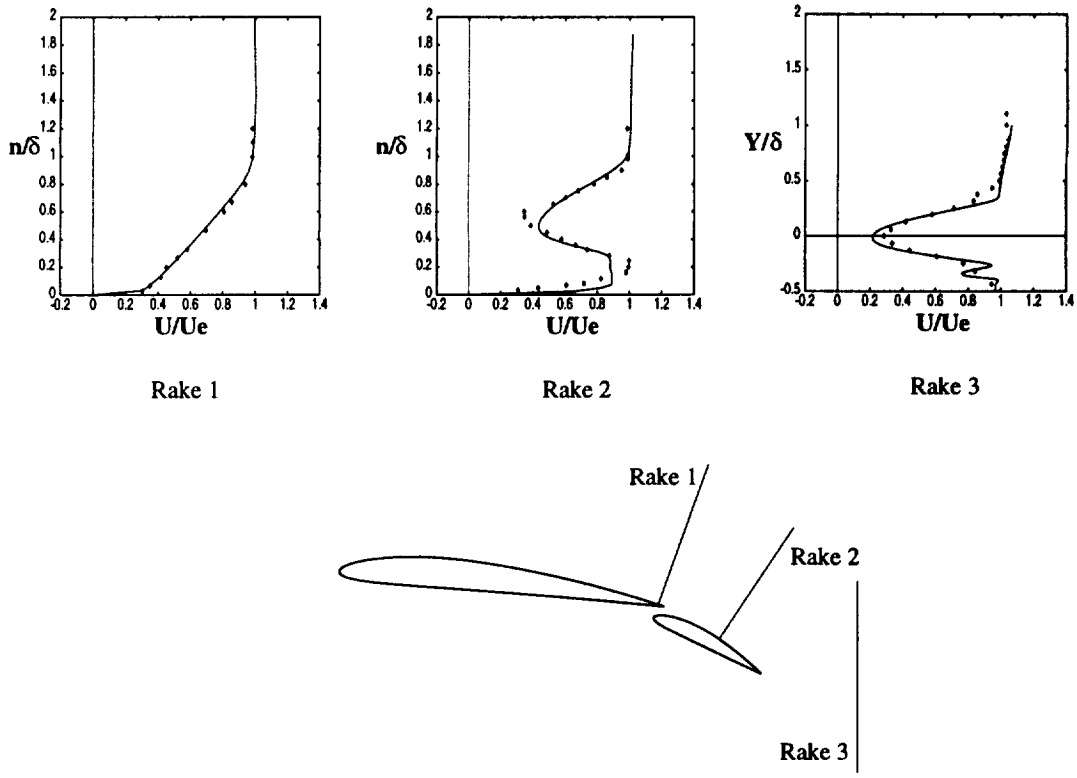

FIGURE 6. Mean velocity profiles: ——— : computed results; ♦: measured data.

outlet are approached the pressure levels become constant. This shows that the computational domain was large enough.

3.3.2 Mean flow: velocity

The mean velocity was measured at three locations using a hot-wire anemometer and a 3-D laser velocimeter. The comparison between computed and experimental x-component velocity is reported in Fig. 6.

The agreement is very encouraging even if there is a difference between computed and measured flap boundary layer thickness. Comparisons with previous results by Rogers (1993) confirm that the main differencies are related to a different gap velocity off the surface of the flap leading edge. It is necessary to point out that in the numerical model no transition trips are mounted on the flap and, therefore, the development of the turbulent boundary layer is not the same as in the experiments.

3.3.3 Turbulence results

The evolution of the turbulent boundary layer on the flap surface can be analyzed from Fig. 7, where the tangential skin friction is reported. The model is capable of capturing the laminar/turbulent transition automatically as it is evident from the skin friction rise in the leading edge region. In the work by Lien *et al.* (1996)

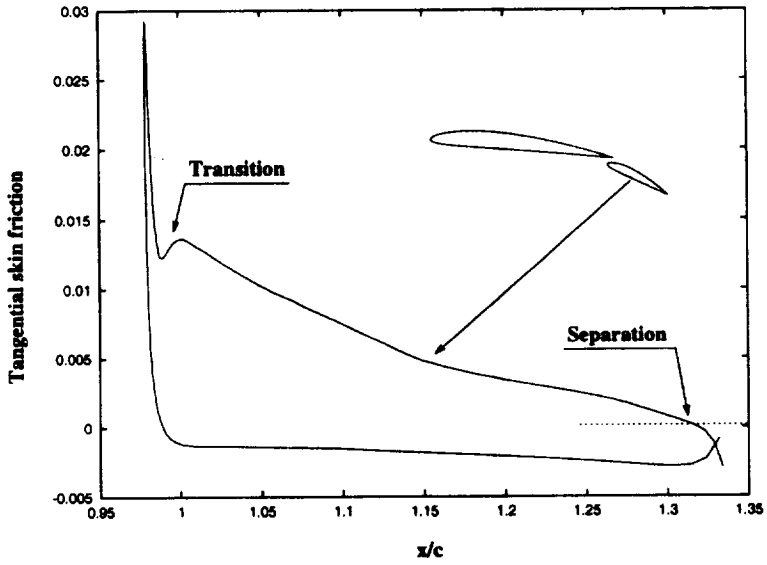

FIGURE 7. Computed tangential skin friction on the flap surface.

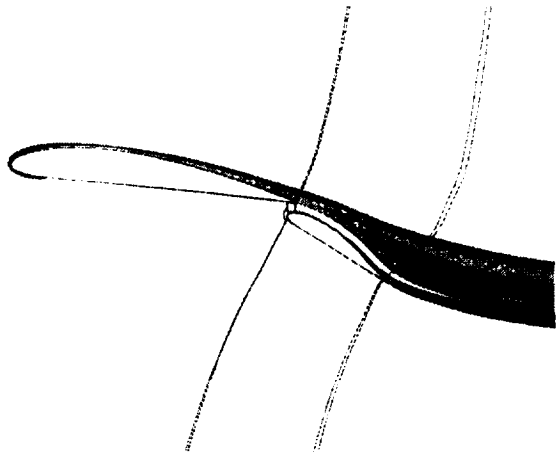

FIGURE 8. Turbulent kinetic energy contours.

the transitional flow in turbomachinery was investigated and the capability of the $k-\varepsilon-\overline{v^2}$ were stressed in detail.

In Fig. 8 the turbulent kinetic energy contours are reported to show the strong interaction between the main airfoil wake and the inviscid jet coming from the slot. It is also clear that on the lower surfaces of the main and flap the boundary layer is laminar and very thin.

FIGURE 9. Three-element airfoil configuration.

4. Three-component configuration

4.1 Experimental test conditions

The three element airfoil configuration of Fig. 9 was investigated in the Farnborough (UK) wind tunnel by I.R. Moir (private communications) in the frame of the AGARD Working Group 14.

The geometric location of the flap and the slat with respect to the main airfoil was prescribed as:

- slat/wing overlap: $SO = -0.01c$
- slat/wing gap: $SG = 0.02c$
- slat deflection: $\delta_s = 25^o$
- wing/flap overlap: $FO = 0$
- wing/flap gap: $FG = 0.023c$
- flap deflection: $\delta_f = 20^o$

A set of angles of attack were investigated, but relevant measurements correspond to $\alpha = 20^o$. The Reynolds number was $Re = 3.52 \times 10^6$ and a trip was mounted over the main airfoil to control transition to turbulence since the wind tunnel turbulence intensity very low.

Experimental data include pressure surface measurements over the airfoil surface at two spanwise locations on the wind tunnel model to outline the absence of three-dimensional effects.

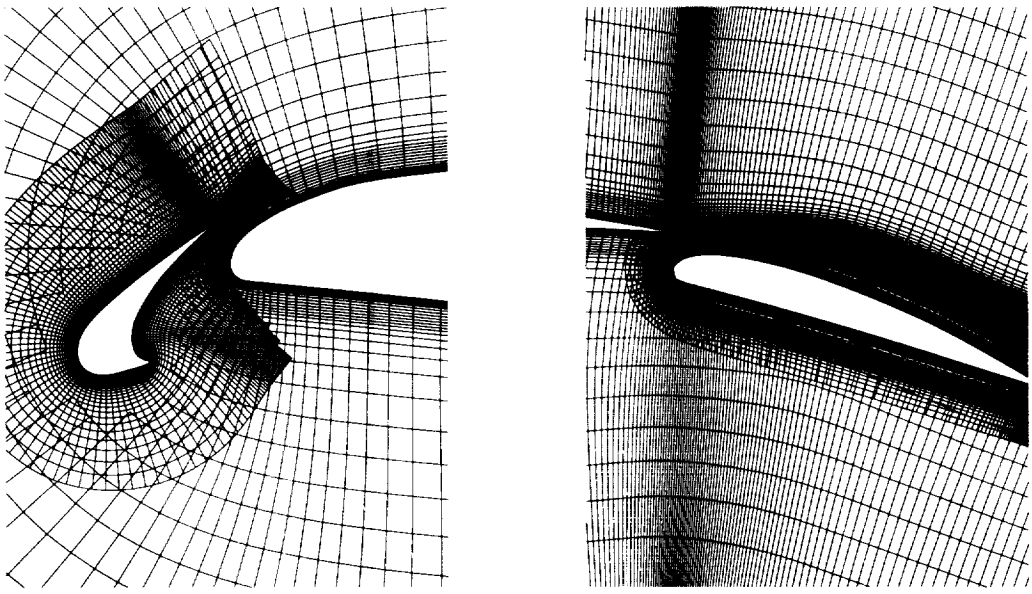

(a) (b)

FIGURE 10. (a) Close-up of the computational grids around the slat; (b) Close-up of the computational grids around the flap.

4.2 Numerical test conditions

The airfoil configuration was defined using the gap and overlap definitions of the preceding section. In this case, the presence of wind tunnel walls was not taken into account, but a correction of the angle of attack (as suggested by the experimental investigators) was adopted: in particular an incidence of $\alpha = 20.18^o$ was used for the computations. The far field boundaries of the computational domain were set to a distance of ≈ 20 chords from the airfoil. The Reynolds number was the same used in the experiment and the flow was assumed to be incompressible. Laminar to turbulent transitions were not fixed.

The computational grid was generated by Rogers (private communication), using three different overlapping zones. Fig. 10 *(a)* reports the mesh around the slat and the main airfoil leading edge, while Fig. 10 *(b)* reports the grid around the main airfoil trailing edge and the flap.

4.3 Results

The pressure distributions over the surface of the three airfoil elements are reported in Fig 11. Comparison with the experimental findings is very promising: the distributions over the main wing and the flap are in very good agreement.

The C_p distribution over the slat presents an overprediction of the suction peak and this is the main discrepancy between experiments and calculations.

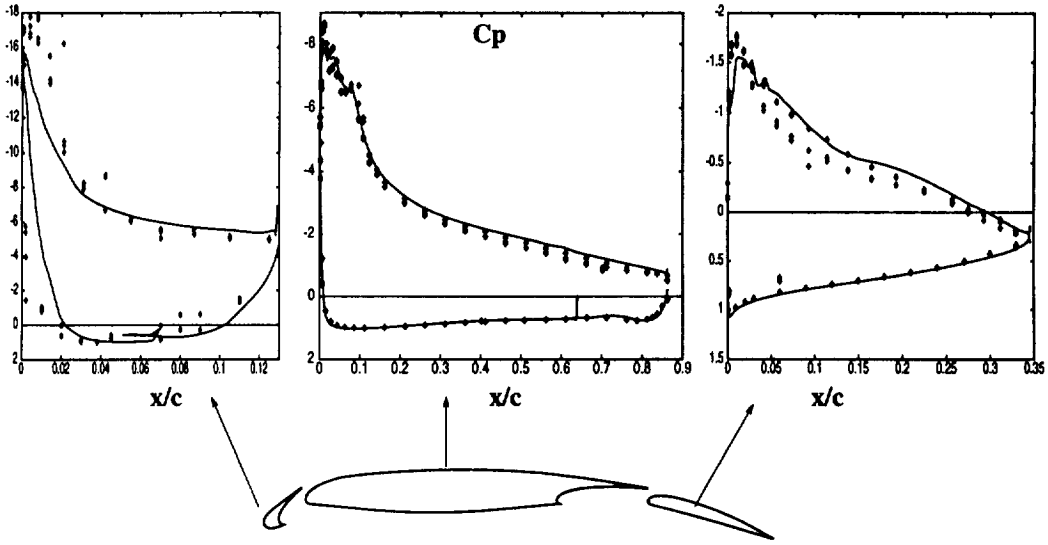

FIGURE 11. Pressure distributions on the airfoil surface. ——— : computed results; ♦: measured data.

REFERENCES

ADAIR, D. & HORNE, W. C. 1989 Turbulent separated flow over and downstream of a two-element airfoil. *Experiments in Fluids.* **7,** 531-541.

DURBIN, P. 1991 Near-wall turbulence closure modeling without 'damping functions'. *Theoretical and Computational Fluid Dynamics.* **3,** 1-13.

DURBIN, P. 1995 Separated flow computations with the $k - \varepsilon - \overline{v}^2$ model. *AIAA Journal.* **33,** 659-664.

LARSSON, T. 1994 Separated and high-lift flows over single and multi-element airfoils. *Proceedings of ICAS Conference 1994.* **2505-2518.**

LIEN, F. S., DURBIN, P. 1996 Non-linear $k - \varepsilon - \overline{v}^2$ modeling with application to high-lift. *Proceedings of the Summer Program 1996.* NASA Ames/Stanford Univ.

PAPADAKIS, M., LALL, V. & HOFFMANN K. A. 1994 Performance of Turbulence models for planar flows: a selected review. *AIAA Paper 94-1873.*

ROGERS, S. E., KWAK, D. & KIRIS C. 1991 Numerical solution of the incompressible Navier-Stokes equations for steady-state and time-dependent problems. *AIAA Journal.* **29,** 603-610.

ROGERS, S. E., KWAK, D. & WILTBERGER N. L. 1993 Efficient simulation of incompressible viscous flow over single and multielement airfoils. *Journal of Aircraft.* **30,** 736-743.

ROGERS S. E., MENTER F. R., DURBIN P. A. & MANSOUR N. N. 1994 A comparison of turbulence models in computing multi-element airfoil flows. *AIAA Paper 94-0291.*